remote sensing

MDPI

Article

Latitude-Dependent Ionospheric Dynamics During the Moderate Geomagnetic Storm of 21–22 March 2026 over the Indian Longitude Sector

Imdad Rizvi [1,*], Siva Sai Kumar Rajana [2,3], Chiranjeevi G. Vivek [2], Punyawi Jamjareegulgarn [4] and Sampad Kumar Panda [3]

[1] Electrical Engineering Division, Sharjah Campus A (SJA), Higher Colleges of Technology, University City, Sharjah P.O. Box 7946, United Arab Emirates
[2] CSIR-National Institute of Data Science and AI (CSIR-NIDSA) (Erstwhile CSIR Fourth Paradigm Institute), Bangalore 560037, India; sivasai7552081@gmail.com (S.S.K.R.); vivek@csir4pi.in (C.G.V.)
[3] Department of Electronics and Communication Engineering, Koneru Lakshmaiah Education Foundation, Green Fields, Vaddeswaram 522302, India; sampadpanda@kluniversity.in
[4] King Mongkut's Institute of Technology Ladkrabang, Prince of Chumphon Campus, Chumphon 86160, Thailand; punyawi.ja@kmitl.ac.th
* Correspondence: irizvi@hct.ac.ae; Tel.: +971-504786022

Highlights

What are the main findings?

- The moderate geomagnetic storm during 21–22 March 2026 produced strongly latitude-dependent and contrasting ionospheric responses over the Indian longitude sector, with simultaneous positive effects at mid-latitudes and negative effects near the equatorial ionization anomaly (EIA) crest during the main phase.
- Combined observations from GNSS and Swarm constellations show that prompt penetration electric fields (PPEFs), storm-time neutral winds, and thermospheric composition changes (O/N2) jointly controlled the evolution of TEC and electron density during the storm and recovery phases.

What is the implication of the main finding?

- Ionospheric disturbances even during moderate geomagnetic storms cannot be represented by a uniform regional response over the equatorial and low-latitude regions, emphasizing the latitude-dependent modelling of plasma dynamics.
- The results support the efforts for improving the forecasting and mitigation of geomagnetic-storm impacts on GNSS navigation and communication systems, particularly across low- and mid-latitude regions.

Check for updates

Academic Editors: Si Chen and Serdjo Kos

Received: 11 August 2026
Revised: 24 September 2026
Accepted: 30 September 2026
Published: 23 October 2026

Copyright: © 2026 by the authors. Licensee MDPI, Basel, Switzerland. This article is an open access article distributed under the terms and conditions of the Creative Commons Attribution (CC BY) license.

Abstract

This study examines the highly variable and latitude-dependent ionospheric response to the moderate geomagnetic storm that occurred on 21–22 March 2026 over the Indian longitudinal sector using combined observations of Global Navigation Satellite System (GNSS) derived Total Electron Content (TEC) and Swarm electron density profiles. During the main phase on 21 March, pronounced positive ionospheric storm effects were observed at mid-latitudes, with Vertical TEC (VTEC) enhancements reaching up to 35 TECU, while notable negative storm effects occurred near the Equatorial Ionization Anomaly (EIA) crest region. These simultaneous observations from mid-latitude and EIA regions are attributed to the combined effects of Prompt Penetration Electric Fields (PPEFs) and the possible presence of storm-induced equatorward neutral winds. The low-latitude region exhibited

moderate daytime ionospheric variations throughout the storm period, despite the presence of PPEFs. Interestingly, electron density profiles from Swarm-A and Swarm-C satellites showed a reduction around the EIA region, along with elevated electron densities near the magnetic equator during the evening period of the storm main phase. On 22 March, the storm-time ionospheric response transitioned into a more complex mixed pattern, with recovery to near-quiet levels at most stations. Moderate VTEC enhancements in the EIA region and distinct mid-latitude electron density increases are likely attributed to the thermospheric composition changes characterized by an increased O/N2 ratio. These findings highlight the synergistic roles of electrodynamic forcing, neutral wind circulation, and altered thermospheric composition in modulating storm-time ionospheric behavior. This study provides valuable insights into complex plasma dynamics at low- and mid-latitudes, with important implications for GNSS-based navigation and communication systems during geomagnetic disturbances.

Keywords: ionosphere; geomagnetic storm; total electron content; thermosphere; PPEFs; equatorward neutral wind

1. Introduction

Geomagnetic storms are one of the most significant space weather phenomena, which occur due to the complex interactions between solar wind disturbances of Coronal Mass Ejections (CMEs) and High-Speed Solar Wind Streams (HSS) with Earth's magnetosphere [1–3]. These storms are characterized by a rapid and pronounced decrease in the horizontal component of Earth's geomagnetic field. The energy input during geomagnetic storms affects the coupled Magnetosphere–Ionosphere–Thermosphere (MIT) system, and this coupling leads to significant modifications in ionospheric parameters, including electron density, Total Electron Content (TEC), and plasma drift patterns [4]. At low- to mid-latitudes, this response is particularly complex due to the presence of the equatorial ionization anomaly (EIA), where the equatorial fountain effect driven by the eastward electric field redistributes plasma from the magnetic equator toward the anomaly crests (~±15 magnetic latitude) on both hemispheres [5].

Ionospheric dynamics during geomagnetic storms are complex and can manifest in both positive and negative phases. Positive storm phases are characterized by enhancements in electron density and TEC, which are primarily driven by PPEFs and changes in neutral composition [6–10]. In particular, PPEFs enhance equatorial upward plasma drifts and intensify the fountain effect, leading to positive ionospheric storms that often extend from low- to mid-latitudes [11,12]. Conversely, negative storm phases involve reductions in electron density, which are linked to Disturbance Dynamo Electric Fields (DDEFs) and changes in thermospheric composition that affect ionospheric recombination rates [13,14]. Thermospheric heating at high latitudes contributes to compositional changes and equatorward-propagating meridional winds that modulate electron density [15,16]. Additionally, PPEFs and DDEFs influence Traveling Ionospheric Disturbances (TIDs), Equatorial Spread-F (ESF) irregularities, and GPS scintillations. These storm-time effects can disrupt satellite operations, communication systems, navigation accuracy, and power grids on Earth [17]. Therefore, understanding the temporal and spatial evolution of geomagnetic storms and their ionospheric impacts is critical for mitigating their adverse effects.

The ionospheric response to geomagnetic storms has been extensively investigated over several decades, ranging from storm-time electric fields inducing electrodynamic variations to changes in thermospheric composition. Fuller-Rowell et al. (2002) [18] used a

3D coupled model to analyze the low-latitude thermosphere–ionosphere responses during the geomagnetic storm and revealed that electrodynamic changes dominate over molecular composition effects. The storm-induced high-latitude energy deposition alters the global circulation and wind patterns and produces rapid equatorial ionospheric changes. Vijaya Lekshmi et al. (2008) [19] investigated the primary drivers of positive ionospheric storms at low- to mid-latitudes during the geomagnetic storm of November 2004. They revealed that PPEFs and equatorward neutral winds have combined effects on the electron density (NmF2) and TEC, shifting ionization anomaly crests and enhancing ionospheric densities at mid-latitudes. Wang et al. (2010) [20] compared the ionospheric variations during three geomagnetic storms using GPS-TEC data and CMIT model simulations, revealing consistent features of enhanced TEC at low/mid-latitudes and depleted TEC near the geomagnetic equator. The primary driver of these effects is identified as storm-time eastward electric fields. Additionally, high-latitude negative storms are linked to molecular nitrogen increases, while equatorial negative responses result from plasma transport rather than thermospheric composition changes. Nava et al. (2016) [21] studied the ionospheric variations during the 2015 St. Patrick's Day storm across different longitudinal sectors using global and regional TEC data. The initial storm phases showed one or two positive ionospheric storm effects that varied with longitude. The American sector experienced the most pronounced increase in VTEC, whereas the Asian sector showed the largest VTEC decrease. Bojilova and Mukhtarov (2023) [22] investigated the spatial and temporal patterns of TEC anomalies globally and regionally during the geomagnetic storm of 3–4 February 2022 using ionosonde and TEC data. They identified the distinct regional mechanisms affecting ionospheric electron density, which include particle precipitation in polar sectors, O/N2 ratio changes at mid-latitudes, and electric field influences near the geomagnetic equator. Rukundo (2023) [23] reported the ionosphere variations during the November 2021 geomagnetic storm using the GNSS TEC, ionosonde, and modeled wind velocities over Africa. They reported distinct positive/negative storm effects linked to PPEFs and TIDs, with regional variations driven by thermospheric composition changes.

In the Indian region, numerous case studies have highlighted the pronounced ionospheric variations during geomagnetic storms [24–30]. Sreeja et al. (2009) [24] analyzed the equatorial ionospheric variations during geomagnetic storms in January 2005. They highlighted that westward DDEFs inhibited EIA development and ESF occurrence on two storm days, whereas eastward PPEFs delayed EIA development and weak ESF onset, which was accompanied by a distinctive F3 layer. Simi et al. (2012) [25] examined equatorial ionospheric variations during a geomagnetic storm on 8–10 November 2004, using ionosonde, magnetic field, and GUVI O/N2 data. They highlighted the significant influence of storm-induced O/N2 variations, PPEFs, and DDEFs in modulating the EIA over the Indian region. The findings revealed complex interactions affecting ionization distribution, with varying effects observed across different locations and days. Chakraborty et al. (2015) [26] reported significant storm-time VTEC variations during the 24 April and 15 July 2012 geomagnetic storms, with enhancements up to 150% at the equatorial station (Port Blair) and depressions up to 72% at the EIA crest (Agartala). They highlighted the dominant role of electrodynamic processes (PPEFs and DDEFs) over mechanical effects (storm-induced equatorward neutral winds and thermospheric composition changes) and revealed the striking contrast in storm impact between the equatorial and EIA regions along the same longitude. Paul et al. (2020) [27] investigated the ionospheric dynamics during a geomagnetic storm occurred in December 2015 over low- and mid-latitudes. Significant TEC variations were observed during the main phase of the storm due to PPEFs, with mid-latitude TEC returning to normal during post-storm period, while low-latitude TEC remained elevated for two days. Thermospheric O/N2 data and CTIPe model simulations

aligned with the observed results, except for the anomalous low-latitude behavior on 22 December, which was influenced by local dynamics and plasma transport. Rajana et al. (2024) [29] examined the ionospheric changes during March and April 2023 geomagnetic storms and revealed distinct latitude-dependent effects, with positive storm phases near the equator and negative phases at EIA, mid-latitudes during the storm recovery phase, primarily driven by westward DDEFs. Chougule et al. (2026) [30] investigated the unusual ionosphere variations during the June 2025 summer solstice geomagnetic storm and revealed pronounced positive storm effects, which included the significant poleward expansion of the EIA. The positive storm effects were primarily driven by PPEFs and equatorward meridional winds. The storm later transitioned into the negative phase, which was dominated by DDEFs and thermospheric composition changes.

Despite numerous advanced studies, significant gaps remain in our understanding of ionospheric variations, particularly regarding the timing, magnitude, and complex interplay of the underlying physical mechanisms during individual geomagnetic storms. Global models often struggle to deliver accurate predictions over the Indian low-to-mid-latitude region, largely due to data sparsity and the region's unique electrodynamics. These limitations highlight the continued need for detailed regional case studies using multi-instrument observations. The present study investigates the latitudinal variations in ionospheric dynamics during a moderate geomagnetic storm that occurred 21–22 March 2026 along the Indian longitude sector on, using multi-instrument observations. These findings are new and previously unreported and provide new insights into the complex interplay between electric fields and neutral wind changes.

2. Materials and Methods

This study used dual-frequency GPS observations from six GNSS stations operated by the IGS and CSIR-National Institute of Data Science and AI (CSIR-NIDSA) observational networks in India (Table 1 and Figure 1). These stations are strategically aligned in the latitudinal transect, spanning geomagnetic latitudes from approximately 2°N to 35°N. This latitudinal alignment covers the key ionospheric zones over the Indian longitudes, including near the geomagnetic equator, the low-latitude, (EIA), and mid-latitude regions.

Table 1. Geographic and geomagnetic coordinates of GNSS stations used in this study.

Station Place/Code	Geog. Lat (°N)	Geog. Long (°E)	Geomag. Lat. (°N)	Geomag. Long. (°E)	Operating Agency
Kodaikanal/KODI	10.23	77.46	2.15	150.61	CSIR-NIDSA
Bangalore/IISC	13.02	77.57	4.90	150.94	IGS
Bhopal/BHPL	23.29	77.28	15.09	151.60	IGS
Dehradun/DRDN	30.34	78.04	22.05	152.94	IGS
Leh/RSC1	34.13	77.60	25.80	152.80	CSIR-NIDSA
Poligan/POL2	42.68	74.69	34.56	151.12	IGS

Slant TEC (STEC) was derived from the raw GPS pseudorange and carrier-phase observations (30-s interval) using GPS-TEC analysis software (Version 3.5) [31]. The software performs carrier-phase levelling, detects and corrects cycle slips, and applies satellite and receiver bias corrections. STEC values were converted to VTEC by applying a mapping function, assuming an ionospheric shell height of 350 km (HIPP).

An elevation cut-off angle of 20° was selected to reduce the effects of multipath and errors associated with the lower atmosphere.

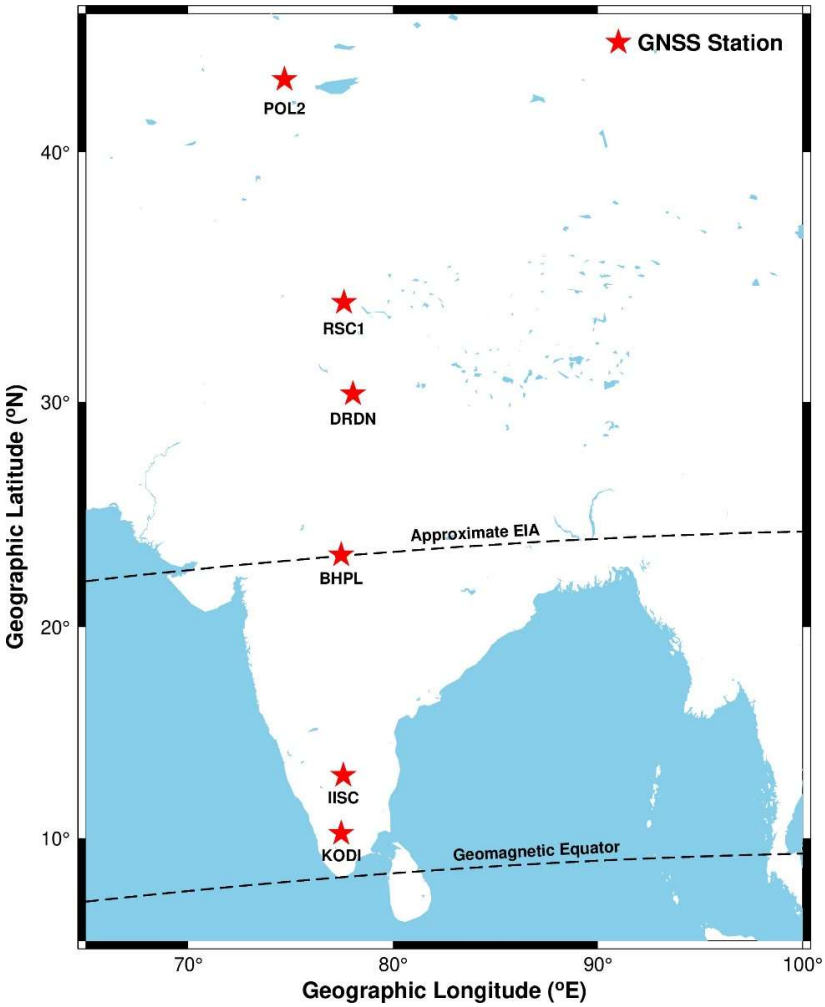


Figure 1. Locations of the GNSS stations in the Indian longitude sector considered in this study.

In addition, in situ electron density (Ne) (Level-1B plasma data) profiles were obtained from ESA Swarm satellites. The Swarm constellation operates in a low Earth orbit at altitudes of approximately 450–530 km, providing high-resolution measurements along the satellite tracks [32]. Thermospheric O/N2 data were acquired from the GUVI onboard TIMED satellite. These measurements offer insights into thermospheric composition, where increases in O/N2 indicate oxygen-rich conditions favorable for enhanced electron density, while decreases signify molecular nitrogen enhancement associated with storm-time upwelling and negative ionospheric storm effects. To investigate the role of storm-time electrodynamical processes, electric fields derived from the PPEF model are included in this study. This empirical transfer function model, driven by Interplanetary Electric Field (IEF) inputs, estimates the penetration electric fields into the equatorial and low-latitude ionosphere [33].

3. Results

3.1. Temporal Variations of Geomagnetic and Interplanetary Parameters from 20–25 March 2026

Figure 2 presents the temporal variation of geomagnetic indices and interplanetary parameters from 20 to 25 March. Prior to the major geomagnetic storm disturbances at 1800 UT on 20 March, the AE index remained below 600 nT, and the ASY-H, SYM-H, and Kp indices were relatively quiet during the period. After 1800 UT on 20 March, a major geomagnetic disturbance developed, and the AE index intensified rapidly, exhibiting multiple intense substorms that frequently exceeded 1000 nT and peaked above 2400 nT during

the main phase on 22 March. This enhanced auroral electrojet activity was accompanied by an increase in the ASY-H index, which rose to nearly 200 nT and displayed multiple fluctuations, which indicated a strongly asymmetric ring current. Concurrently, the SYM-H index showed a pronounced main phase decrease on 21 March and reached a minimum value of approximately—120 nT around 0000 UT on 21 March and 1600 UT on 22 March, followed by a prolonged recovery phase. These geomagnetic responses coincided with enhanced solar wind–magnetosphere coupling, evidenced by repeated southward turnings of the IMF Bz component, which reached a minimum value of approximately −30 nT at around 0000 UT on 21 March. This coupling is further shown by several large positive excursions in the interplanetary electric field Ey, which reached a value of approximately 13 mV/m, with intensification beginning after 1800 UT on 20 March. Correspondingly, the Kp index increased from values ≤ 3 to levels between 5 and 7 starting on 20 March, remaining elevated for nearly two days before gradually declining toward moderate activity on 24 March. Collectively, these parameters showed a significant geomagnetic storm characterized by strong solar wind driving and substantial ring current development.

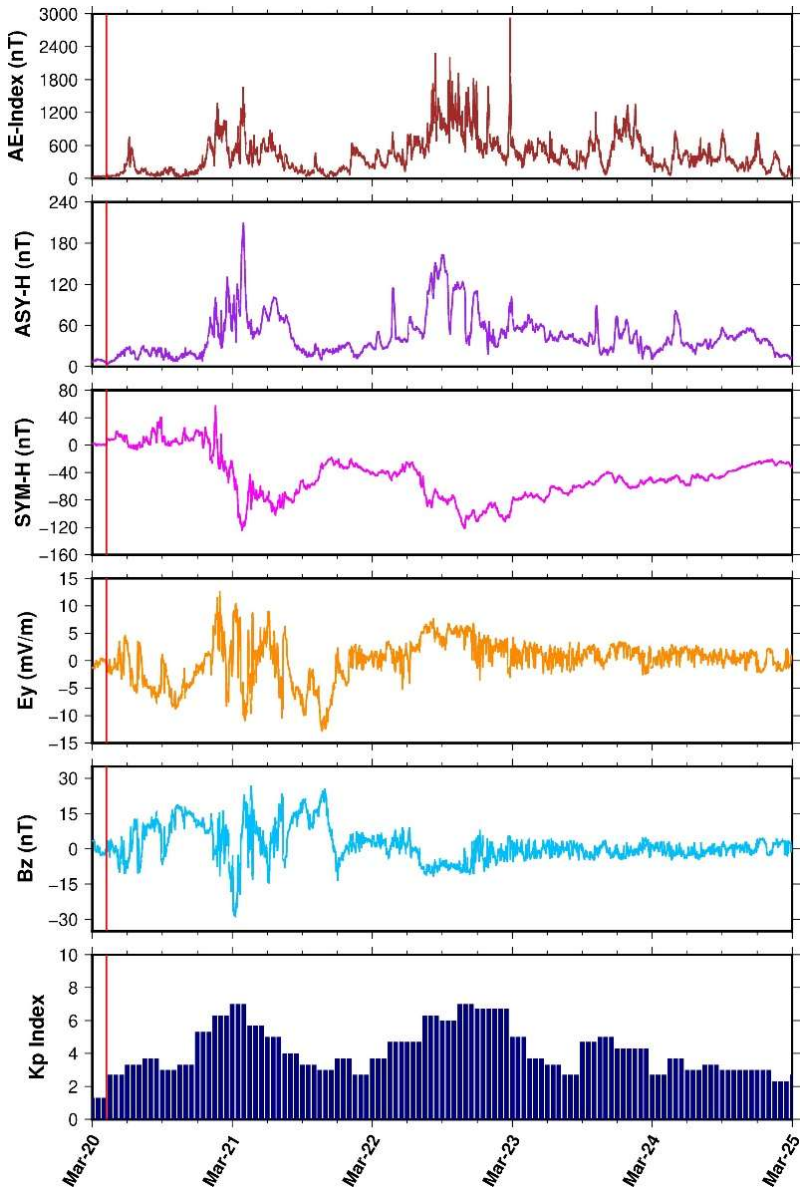


Figure 2. Variations of geomagnetic and interplanetary parameters during 20–25 March 2026. The red line indicates the storm onset time.

3.2. Diurnal Variations of GPS-Derived VTEC During the Storm Period

Figure 3 shows the diurnal variation of VTEC observed at six latitudinally aligned GNSS stations spanning low- to mid-latitudes geomagnetic regions as listed in Table 1. The black curve and green shading denote the monthly quiet-day average VTEC determined from the five International Quiet Days (IQDs) (02, 05, 17, 18, and 19) of the month and its standard deviation error bars during March 2026, defining the quiet-time VTEC baseline used in the analysis. The IQDs are published on the World Data Center for Geomagnetism, Kyoto website (https://wdc.kugi.kyoto-u.ac.jp/qddays/) (accessed on 2 June 2026).

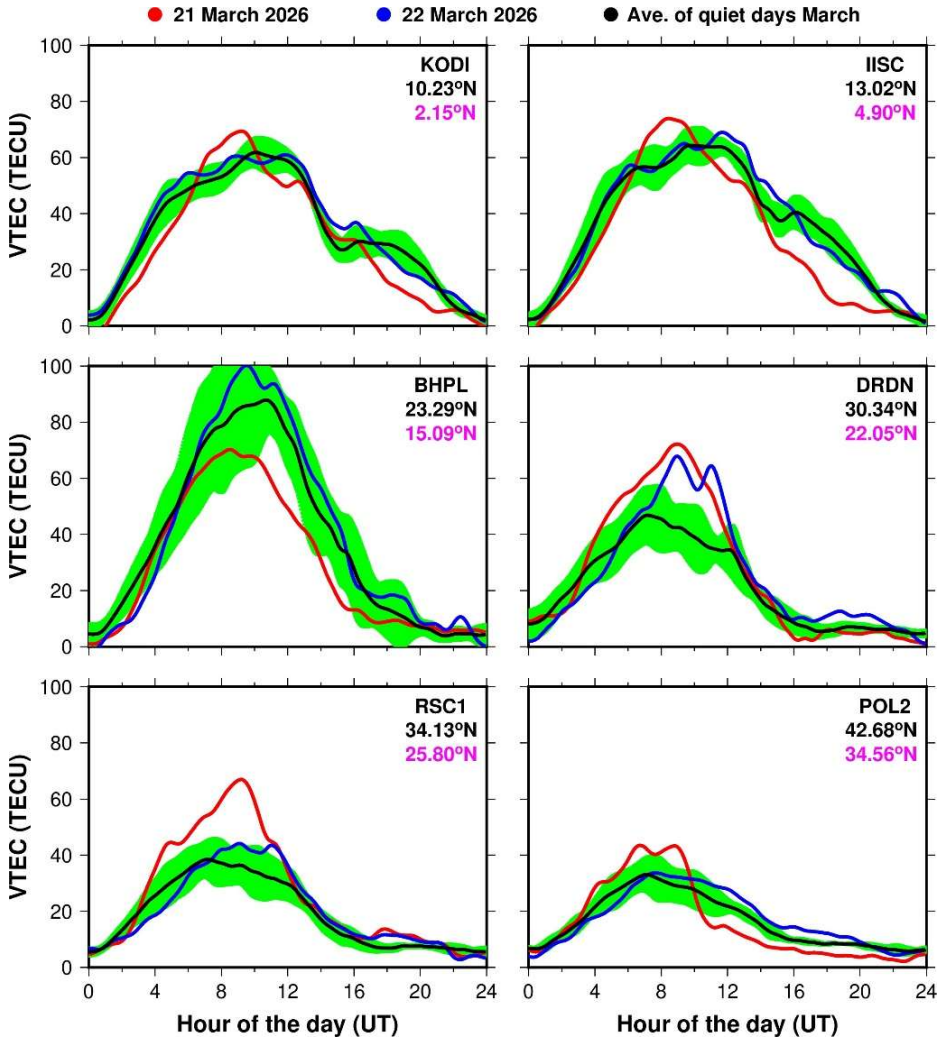


Figure 3. Diurnal variations of GPS-derived VTEC on 21 March (red) and 22 March (blue), and average VTEC (black) during March 2026 along with the standard deviation error bars (green).

The corresponding differential TEC (dTEC = Storm-day VTEC—Quiet-day average VTEC) at each station is shown in Figure 4.

It is clear from Figure 3 that on 21 March (red curve), a pronounced positive ionospheric storm is evident at the mid-latitude stations DRDN, RSC1, and POL2. However, at DRDN, the VTEC peaked to ~72 TECU near 0920 UT, against the quiet-day peak of ~45 TECU. The corresponding dTEC enhancement at this location reached the maximum value of ~+30 TECU from 0800 to 0900 UT, sustaining above a threshold value of +15 TECU for about 4 h. Similarly, the VTEC value at RSC1 reached the maximum of ~67 TECU near 0900–1000 UT compared to the quiet-day peak of ~38 TECU, with dTEC abruptly rising to a maximum limit of ~+30 TECU around 0900–1000 UT. At POL2, VTEC reached a

maximum of ~44 TECU near 0800 UT against the quiet-day peak of ~33 TECU, with dTEC peaking at ~+14 TECU around 0800–0900 UT, before falling to the negative excursion of ~−8 TECU around 1600–1800 UT. In contrast, the low-latitude stations KODI and IISC exhibited modest daytime enhancements. At KODI, VTEC increased near 0800–0900 UT against the quiet-day peak (dTEC ≈ +13 TECU, lasting around 3 h), while at IISC, VTEC increased above ~75 TECU near 0800–0900 UT above the quiet-day peak of ~62 TECU (dTEC ≈ +16 TECU). The two low-latitude stations subsequently developed a pronounced negative deviation later in the day, with dTEC dropping to ~−15 TECU at KODI (around 1800–1900 UT) and to ~−22 TECU at IISC (around 1800 UT). In particular, the station nearest the EIA crest (BHPL) recorded a marked decrease in VTEC compared to quiet-time levels. The VTEC peaked at only ~68–70 TECU compared to the quiet-day peak of ~87 TECU, with dTEC dropping to the minimum value of ~−29 TECU near 1100 UT and attaining below −15 TECU from 0800 to 1600 UT.

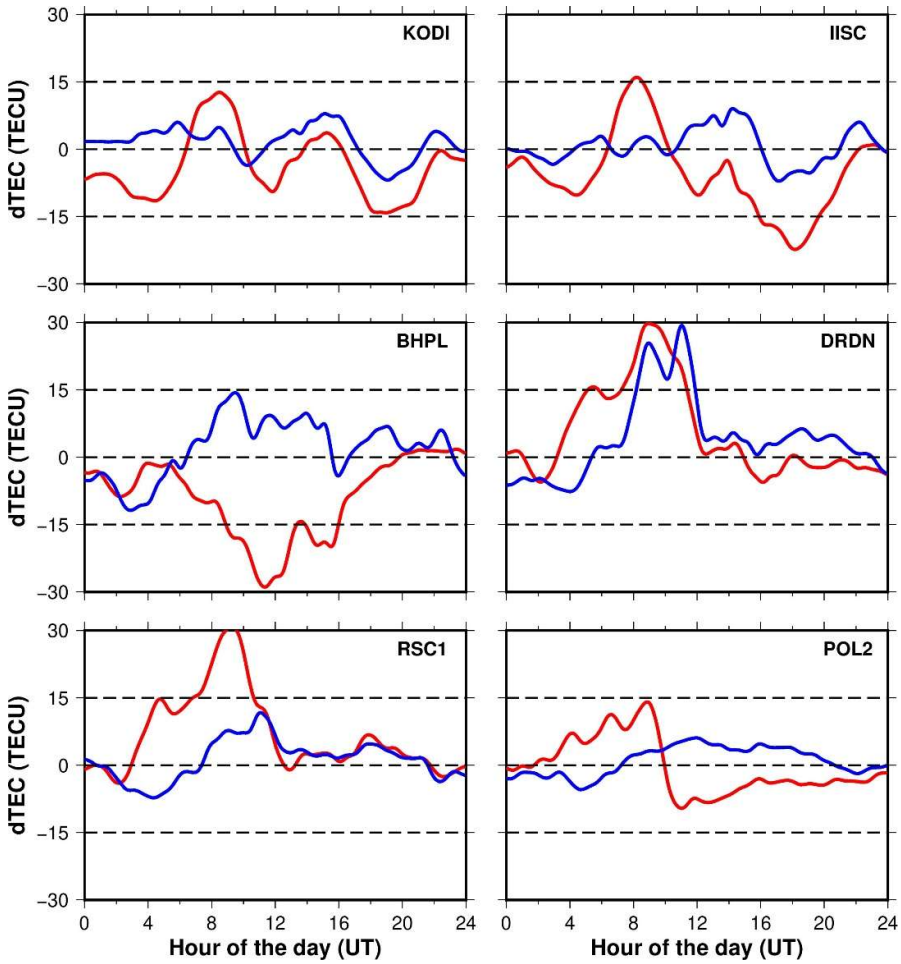


Figure 4. Temporal variations of dTEC during the geomagnetic storm conditions on 21 March (red) and 22 March (blue).

On 22 March 2026 (blue curve), the storm-time response seems to be more complex due to the intermixing of different storm-time phenomena. At the low-latitude stations, VTEC and dTEC remained close to the quiet-day baseline: KODI showed a small positive dTEC of no more than ~+8 TECU, and IISC oscillated between about −5 and +10 TECU. The mid-latitude stations RSC1 and POL2 also exhibited comparable VTEC values to those of the quiet-day baseline, with dTEC not exceeding ~+12 TECU at RSC1 and ~+6 TECU at POL2. The station in the vicinity of the approximate EIA crest region (BHPL) showed a modest positive enhancement, with VTEC reaching ~100 TECU (quiet-day peak ~87 TECU)

and dTEC peaking at ~+15 TECU around 0800 UT. The magnitude of VTEC was sustained between almost +5 and +10 TECU through 1600 UT, in contrast to the pronounced VTEC depletion recorded at this station on 21 March. Notably, a distinct double-peak enhancement is recorded at the mid-latitude station DRDN, where VTEC reached ~65–68 TECU (quiet-day peak ~47 TECU) with dTEC rising sharply to ~+25 TECU near 1000 UT and a maximum level of ~+30 TECU near 1100 UT.

The VTEC observations during the two geomagnetic storm days revealed a clear latitudinal gradient in the ionospheric response. On 21 March, the strongest positive storm phase (dTEC up to +30 TECU) occurred in the mid-latitude region (DRDN, RSC1), weakening towards higher mid-latitude POL2 (+14 TECU) and the low-latitude stations (+13 to +16 TECU), by transitioning through the pronounced negative phase (dTEC down to −29 TECU) at the EIA crest station BHPL. On 22 March, positive storm effects persisted mainly at the EIA-crest latitude (BHPL; dTEC up to +15 TECU) and low-to-mid-latitude transitional location (DRDN; dTEC up to +30 TECU), whereas the low-latitude locations (KODI, IISC) and higher mid-latitude locations (RSC1 and POL2) showed only minor deviations from their respective quiet-day baselines. These differential effects on VTEC are likely attributed to the combined influence of PPEFs, storm-time neutral winds, and changes in thermospheric composition during the geomagnetic storm. These TEC variations are further corroborated by the Global Ionosphere Maps (GIMs) shown in Figure 5.

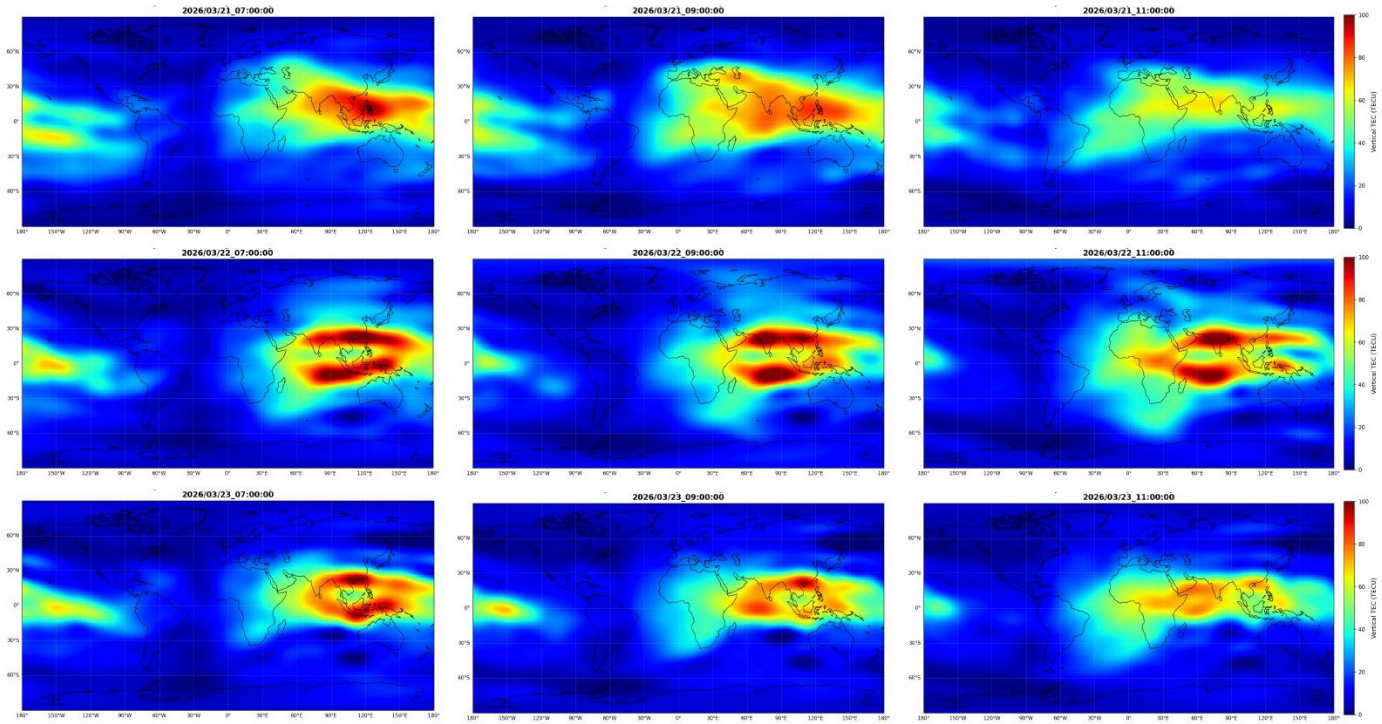


Figure 5. GIM-derived TEC maps during the storm period from 21 to 23 March 2026 (07 UT, 09 UT, 11 UT).

3.3. Variations of the Swarm Satellite-Derived Electron Density Profiles During the Storm Period

Figure 6 shows the orbital tracks and Ne profiles measured by the Swarm-B satellite at daytime during the pre-storm day (20 March) and the geomagnetic storm period (21–22 March). Panel (a) shows the geographic locations of the satellite passes, while panel (b) presents the latitudinal variation of Ne across the Indian longitude sector. Before the storm day (20 March, green curve), the electron density profile exhibited the typical EIA structure with moderate crest-to-trough ratios and peak Ne values around 1.4–1.5 $\times$ 10^6 el/cm^3 near $\pm$15–17°N magnetic latitude. In contrast, during the main phase

of the storm on 21 March (red curve), significant suppression of electron density was observed near the EIA region and reduced crest amplitudes, accompanied by the broadening of the Ne profile in mid-latitude regions. This indicates a negative storm effects in the EIA region and a positive storm effect at mid-latitudes during the storm day. Substantial enhancements in electron density emerged on 22 March (blue curve), and pronounced EIA crests developed with Ne exceeding 1.9×10^6 el/cm^3 at approximately $\pm 18^\circ$ magnetic latitude, showing a clear double-hump structure and significantly elevated densities.

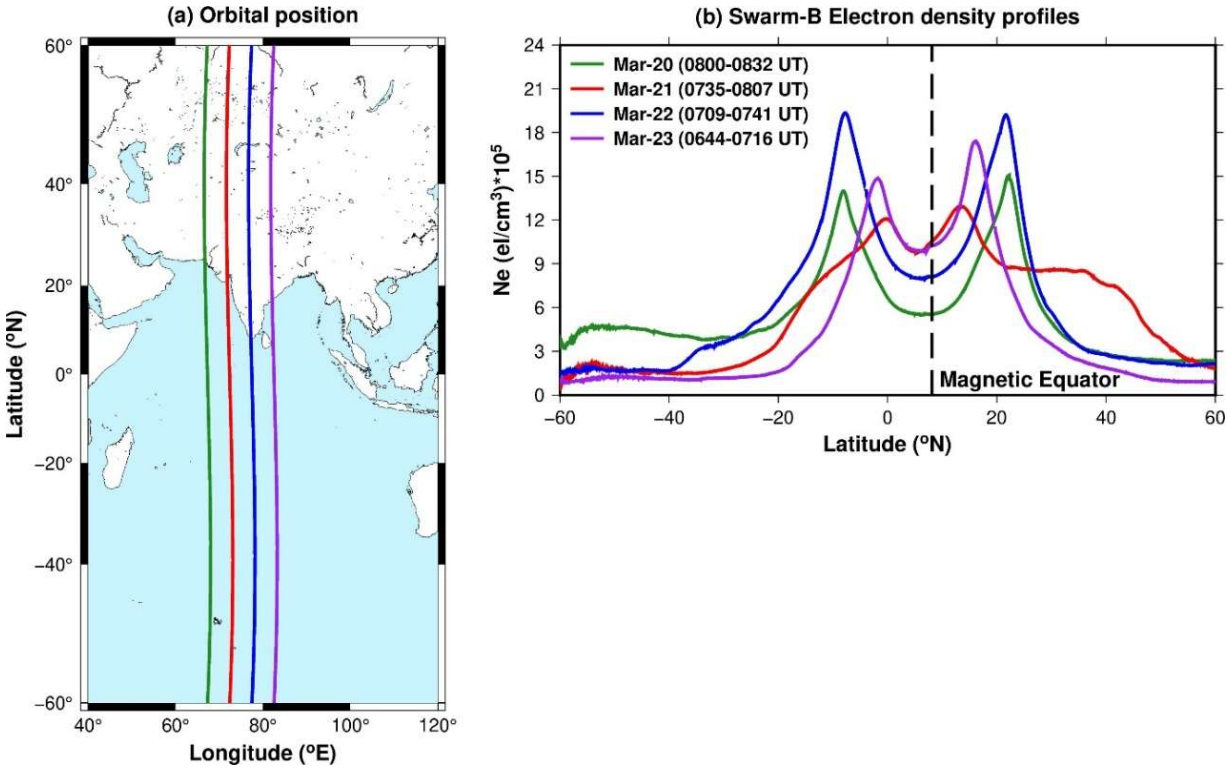


Figure 6. (**a**) The orbital tracks of Swarm-B satellite passes over the Indian longitude sector during 20–23 March 2026 and (**b**) electron density profiles derived from Swarm-B satellite observations. The vertical black dashed line denotes the approximate position of the magnetic equator on the geographic latitude axis.

Figure 7 shows the orbital tracks (panel a) and the corresponding in situ Ne profiles recorded by the Swarm-A (panel b) and Swarm-C (panel c) satellites across the Indian longitudinal sector during 20–23 March 2026. These passes provide complementary observations from the evening sector at slightly different local times and altitudes compared to Swarm-B. On pre-storm day 20 March (green curves) (approximately 68°E), both Swarm-A and Swarm-C exhibited well-developed but moderate EIA structures with crest densities reaching approximately 1.1×10^6 el/cm^3. A noticeable suppression of the EIA structure was observed on 21 March (approximately 73°E) (main phase of the storm), with persistent electron densities near the magnetic equator (red curve in Swarm-A and magenta curve in Swarm-C). In contrast, a drastic enhancement of electron density occurred on 22 March (blue curve in Swarm-A and cyan curve in Swarm-C) (approximately 77°E) (second main phase). Pronounced double-crest EIA structures developed, with peak Ne values exceeding 1.8×10^6 el/cm^3 around 15–20°N, which indicates the strongly amplified equatorial fountain effect. On 23 March (purple curve in Swarm-A and brown curve in Swarm-C), the enhanced EIA persisted during the early recovery phase, although the crest intensities were slightly lower than those observed on 22 March. Collectively, the Swarm constellation observations demonstrated the clear evolution from moderate EIA on

20 March to suppressed and modified conditions during the storm main phase, followed by a moderate positive storm response with markedly intensified EIA crests on 22 March. The marked latitudinal asymmetry and intensification of the anomaly crests on 22 March are consistent with the VTEC enhancements observed at the ground-based GNSS stations (Figures 3 and 5). GNSS VTEC represents the vertically integrated electron content along the entire ionospheric path, whereas Swarm provides local electron density measurements at altitudes of approximately 450–530 km. In the present study, Swarm-B observations were obtained in the local daytime sector (0644–0832 UT) (1214–1352 LT) at longitudes of about 70–85°E, while Swarm-A and Swarm-C observations were acquired in the evening sector (1202–1326 UT) (1732–1856 LT) at longitudes of about 70–90°E. Because of these differences in local time, altitude, and longitude, the Swarm measurements cannot be regarded as a direct quantitative confirmation of the GNSS VTEC variations. Therefore, these datasets are used as supporting qualitative evidence for the spatial and temporal patterns observed in the ground-based VTEC data.

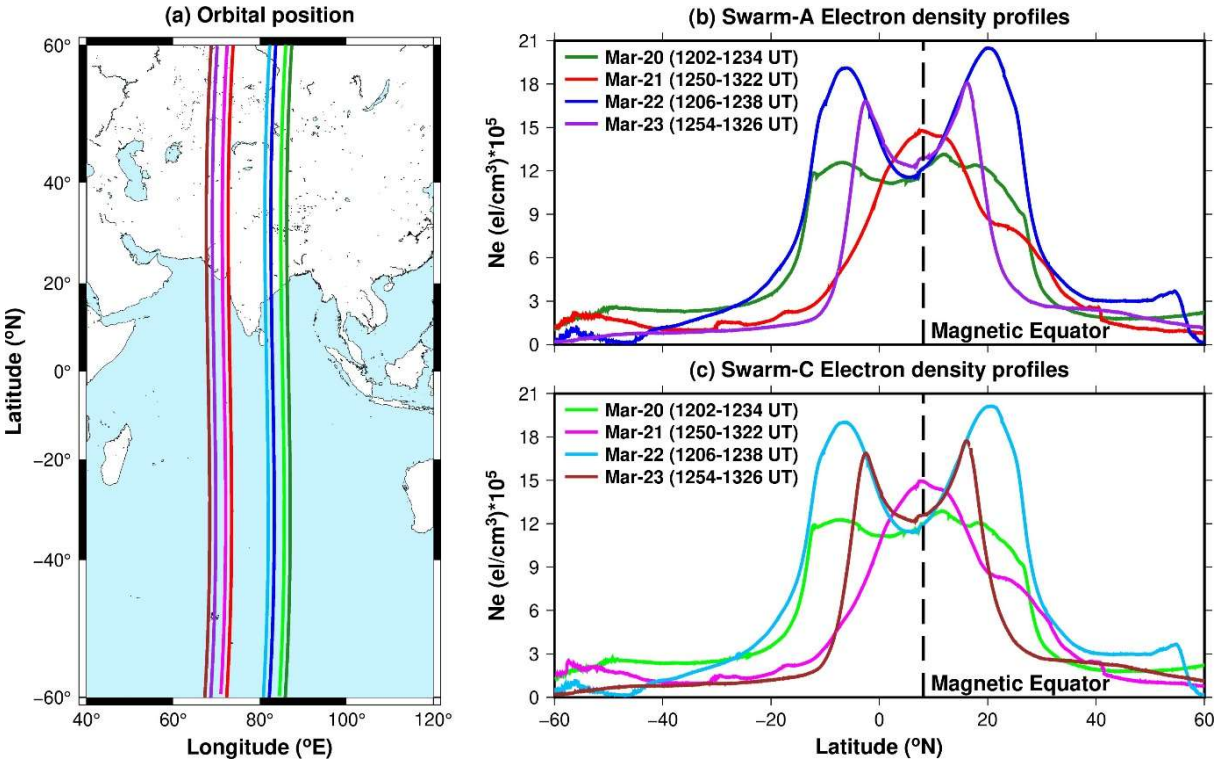


Figure 7. (**a**) The orbital tracks of Swarm-A and Swarm-C satellite passes over the Indian longitude sector during 20–23 March 2026 and electron density profiles derived from (**b**) Swarm-A and (**c**) Swarm-C satellite observations during the storm period from 20 to 23 March 2026. The vertical black dashed line denotes the approximate position of the magnetic equator on the geographic latitude axis.

4. Discussion

Geomagnetic storms play a critical role in modifying the ionospheric environment by affecting plasma density and electron content, which can disrupt communication and navigation systems. The moderate geomagnetic storm on 21–22 March 2026 exhibited pronounced latitudinal ionospheric variability along the Indian longitude sector. During this storm, southward turnings of the IMF-Bz reached approximately −30 nT, and Ey enhanced to 12 mV/m after 1800 UT on 20 March. Concurrently, auroral electrojet activity intensified beyond 2400 nT, with the ASY-H index rising to approximately 200 nT. The SYM-H index dropped to a minimum of −120 nT, and the Kp index increased to values between

5 and 7 during the storm period. This multi-day storm was characterized by prolonged ring current development and enhanced high-latitude currents, which collectively produced significant ionospheric disturbances over the Indian region. During the initial main phase, a pronounced positive ionospheric storm effects were observed at mid-latitudes on 21 March, with VTEC enhancements exceeding the quiet-time levels by up to ~30 TECU. This indicates substantial increases in the storm-time plasma density away from the equatorial and low-latitude regions. These mid-latitude enhancements correspond with the broadening and intensification of electron density profiles measured by the Swarm-B satellite, supporting the effective storm-driven plasma increase in these latitudes. In contrast, the near-EIA crest region at station BHPL showed a notable negative storm effect, with VTEC reductions of 20–25 TECU, reflecting the suppression of the EIA during the storm main phase.

The simultaneous occurrence of positive storm phases at mid-latitudes and negative phases near the EIA during the daytime aligns with established physical mechanisms. Daytime eastward PPEFs enhance the equatorial plasma fountain, causing plasma depletion near the equator and plasma enhancements at higher latitudes [34]. However, PPEFs alone cannot fully develop strong positive storms at mid-latitudes [11,19]. While PPEFs drive upward ExB drifts, removing plasma from the equatorial F-region, the inclined magnetic field lines at mid-latitudes lead to downward diffusion along gravity, resulting in net plasma loss. Conversely, storm-induced equatorward neutral winds may contribute to the positive storm phases at mid-latitudes, as they can reduce downward plasma diffusion and uplift the ionosphere to higher altitudes where recombination rates are lower [6]. These effects peak near ~17° magnetic latitude when winds reach the equator, and produce the positive storms that can extend to lower latitudes. When eastward PPEFs coexist with these winds, the positive response center shifts poleward to more than 25° magnetic latitude [35], which produces the negative phases near the EIA through enhanced plasma outflow [36]. The observed daytime main-phase pattern of mid-latitude enhancements coupled with EIA suppression supports the possible wind-driven mechanism, which is augmented by the presence of PPEFs (Figure 8). During geomagnetic storms, an eastward PPEF that coincides with the developing daytime equatorial electrojet (EEJ) enhances the upward EXB drift over the dip-equatorial region. This strengthens the equatorial fountain effect to redistribute the plasma towards low latitudes, which can lead to enhanced TEC in the equatorial and low-latitude regions. Furthermore, the PPEF model results show that the equatorial electric field exhibited a distinct polarity change on 21 March. The quiet-time electric field (blue) displayed the typical diurnal variation, reaching daytime positive values of approximately +0.7 mV/m and nighttime negative values of about −0.6 mV/m. Superimposed on this, the prompt-penetration component (red) produced a sharp positive spike of ∼0.6 mV/m near the beginning of 21 March, followed by smaller-amplitude fluctuations (±0.2–0.3 mV/m). These elevated positive PPEF amplitudes coincide temporally with the observed daytime VTEC enhancement (Figures 3 and 5) over equatorial and low-latitude regions, supporting the contribution of the eastward penetration electric field to the ionospheric response. In contrast, ionospheric responses at mid and higher latitudes are more likely influenced by storm-time electrodynamic and thermospheric processes, particularly disturbance-driven neutral winds that modify the plasma distribution through changes in the ionospheric dynamo, and neutral wind-induced plasma transport could be considered as a possible contributing mechanism over the region.

A previous study by Lei et al. (2008) [37] observed positive storm effects driven by the combination of electric field perturbations, neutral wind changes, and variations in thermospheric composition. Additionally, Vijaya Lekshmi et al. (2008) [19] highlighted the synergistic role of PPEFs and equatorward neutral winds, which together enhance electron density and TEC, leading to the poleward shift of ionization crests and the notable

increase in mid-latitude plasma densities. Additionally, the electron density profiles from Swarm-A and Swarm-C satellites demonstrated the clear suppression of the EIA structure, with persistently elevated electron densities remaining near the magnetic equator during the evening period. This indicates significant modification of the low-latitude ionosphere under the observed conditions.

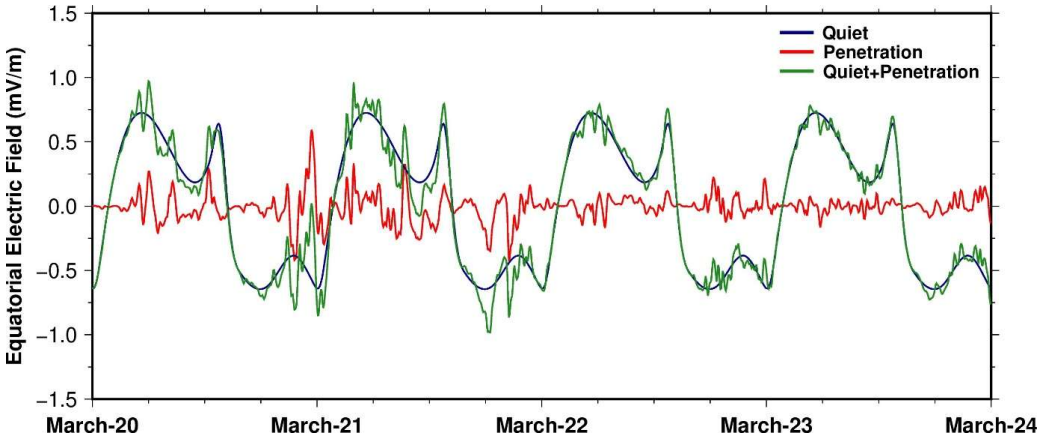


Figure 8. PPEEF model-derived eastward electric fields from 20 to 24 March 2026.

On 22 March, the ionospheric response exhibited a mixed complex pattern. VTEC values at low-latitude stations (KODI, IISC) and mid-latitude stations (RSC1, POL2) returned close to or slightly above the quiet-day baselines, while BHPL recorded moderate VTEC enhancements. The transition from the negative EIA response on 21 March to the positive response on 22 March underscores the time-dependent interplay between electrodynamic forcing and composition changes. A distinct double-peak structure emerged at the mid-latitude station DRDN. Swarm-B in situ electron density profiles corroborated this evolution, revealing peak electron densities exceeding 2.0×10^6 el/cm^3. The EIA region and mid-latitude positive storm effect observed on 22 March is associated with an enhancement in the thermospheric O/N2 ratio (second main phase). GUVI O/N2 maps (Figure 9) show that on 22 March, the O/N2 values over the mid-latitude region from approximately 25 to 40°N in the Indian longitude sector around 1010 UT are clearly elevated relative to the quieter day on 20 March. The storm-time O/N2 ratio in this region reaches values up to ~1.2–1.4, representing a noticeable increase compared with the quiet-time reference levels of ~0.8–1.0 observed on 20 March. The temporal coincidence of these composition changes with the period of elevated GNSS VTEC and Swarm electron density supports the interpretation that the enhanced O/N2 likely contributed to the observed EIA region to mid-latitude positive storm effect on 22 March. Previous studies by Cai et al. (2020) [38] reported that even weak geomagnetic activity can produce significant equatorward expansion of regions with elevated ∑O/N2 ratios, which reduce recombination losses and support higher F-region plasma densities at middle latitudes. Similarly, Yu et al. (2023) [39] analyzed the vertical variations in thermospheric composition during major storms and found O/N2 enhancements at mid- and low-latitudes, primarily driven by decreases in N2 density. Zhang et al. (2014) [40] demonstrated that storm-time O/N2 enhancements frequently extend from high- to mid-latitudes, anti-correlating with NO increases and directly contributing to reduced molecular recombination and elevated TEC. Similarly, Chakraborty et al. (2020) [41] reported that elevated GUVI-derived O/N2 ratios (~0.7) in the low-latitude thermosphere coincided with the strongest positive TEC enhancements during the October 2016 CIR-driven storm over the Indian longitude sector, reinforcing the role of thermospheric compositional changes in modulating ionospheric response. This mechanism is consistent with the present findings, where GUVI-derived

O/N2 enhancements over the low- to mid-latitude sector coincided with the observed VTEC increases during the storm period, suggesting that compositional changes, rather than electrodynamic forcing alone, played the dominant role in sustaining the positive ionospheric response at these latitudes. Additionally, Sur et al. (2022) [42] found strong correlations between GUVI-derived O/N2 variations and mid-latitude VTEC increases, underscoring the critical role of composition changes in modulating ionospheric behavior during geomagnetic storms.

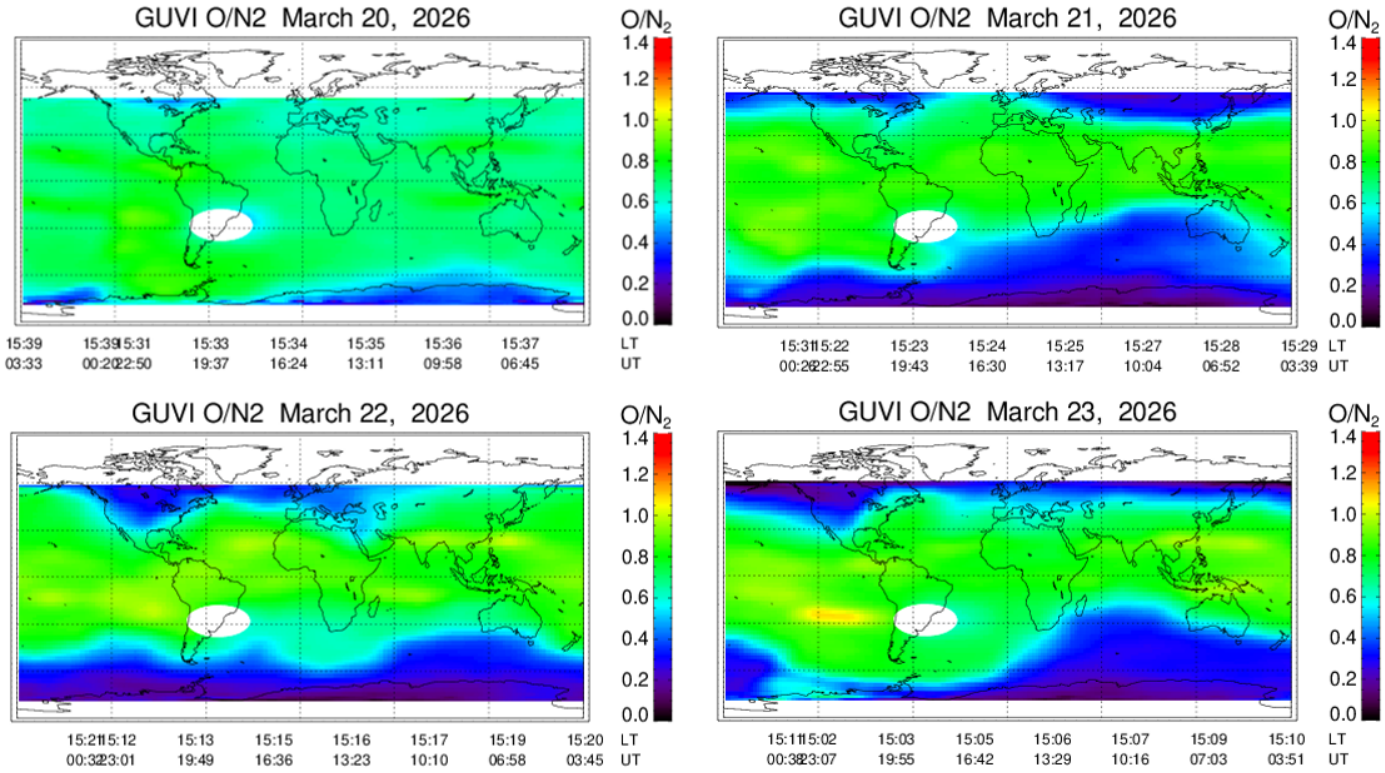


Figure 9. GUVI/TIMED satellite-derived thermosphere O/N2 profiles from 20 to 23 March 2026.

The findings of this study emphasize the critical role of coupled electrodynamic and thermospheric composition in generating latitude-dependent storm effects and highlight the influence of local time, longitude sector, and storm onset conditions in shaping the ionospheric response. Integrating multi-instrument datasets provides a comprehensive framework for understanding these mechanisms over the Indian longitude sector, with important implications for improving ionospheric storm forecasting and mitigating the effects of space weather on navigation and communication systems.

5. Conclusions

The present study investigated the highly variable and latitude-dependent ionospheric response to the moderate geomagnetic storm on 21–22 March 2026 over the Indian longitudinal sector using a combination of ground-based GNSS-derived TEC and in situ electron density measurements from the Swarm satellite constellation.

- A distinct positive ionospheric storm effects were observed at mid-latitudes, and the near-EIA crest region experienced a negative storm effect during the storm main phase on 21 March 2026.
- The simultaneous occurrence of positive mid-latitude and negative EIA ionospheric responses is attributed to the combined influence of daytime eastward PPEFs and the possible presence of storm-induced equatorward neutral winds.

- On 22 March, the ionospheric response became more complex, with mixed VTEC patterns and a shift from negative to positive EIA response.
- The positive ionospheric storm effect observed in the EIA region and the mid-latitude region on 22 March is likely attributed to the enhanced thermospheric O/N2.
- The low-latitude region exhibited moderate ionospheric variations during the daytime of the storm period despite the presence of electric fields (PPEFs) and changes in neutral winds.
- Interestingly, the Swarm-A and Swarm-C electron density profiles showed the suppression of the EIA structure with elevated electron densities near the magnetic equator during the evening period of the storm main phase on 21 March.

This study underscores the importance of coupled electrodynamic and neutral atmospheric processes, local time, longitude sector, and storm onset conditions in shaping latitude-dependent ionospheric storm effects and highlights the value of multi-instrument data integration for understanding storm-time ionospheric behavior over the Indian region.

Author Contributions: Conceptualization, I.R. and S.S.K.R.; methodology, I.R., S.S.K.R. and C.G.V.; software, S.S.K.R. and C.G.V.; validation, I.R., S.S.K.R. and P.J.; formal analysis, I.R. and S.S.K.R.; investigation, I.R., P.J. and S.K.P.; resources, P.J. and S.K.P.; data curation, S.S.K.R. and C.G.V.; writing—original draft preparation, I.R.; writing—review and editing, S.S.K.R. and S.K.P.; visualization, S.S.K.R.; supervision, P.J. and S.K.P.; project administration, C.G.V. and S.K.P.; funding acquisition, C.G.V. and S.K.P. All authors have read and agreed to the published version of the manuscript.

Funding: This work was supported by the National Laboratories Scheme under the ULIP sub-scheme of CSIR-NIDSA project CSIR-NLS/ULIP/CSIR-4PI/MLP002601.

Data Availability Statement: The GNSS RINEX observational and navigational data utilized in this study were downloaded from NASA's Earthdata (https://www.earthdata.nasa.gov/centers/cddis-daac) (last accessed on 2 June 2026). The differential code biases (DCBs) required for processing the GNSS observation data were obtained from the University of Bern archive (https://code.aiub.unibe.ch/) (last accessed on 2 June 2026). European Space Agency Swarm data were accessed through the VIRES web platform (https://vires.services/) (last accessed on 6 June 2026). Real-time eastward equatorial electric field estimates derived from the Prompt Penetration Equatorial Electric Field Model (PPEEFM) were acquired from https://geomag.colorado.edu/online-calculators/real-time-model-ionospheric-electric-fields (last accessed on 8 June 2026). The GUVI/TIMED O/N2 data were downloaded from the GUVI data portal (http://guvitimed.jhuapl.edu/guvi-galleryl3on2) (last accessed on 25 June 2026). NASA JPL Global TEC Maps (GIMs) are obtained from the web portal (https://sideshow.jpl.nasa.gov/pub/iono_daily/gim_for_research/jpld/) (last accessed on 13 September 2026).

Acknowledgments: I.R. is thankful to the Applied Research, Innovation & Entrepreneurship (ARIE) division of Higher Colleges Technology (HCT), UAE, for encouraging this research work. The authors thank the Director, CSIR-National Institute of Data Science and AI (CSIR-NIDSA), Bangalore, India, for supporting the GNSS program.

Conflicts of Interest: The authors declare no conflicts of interest.

Abbreviations

The following abbreviations are used in this manuscript:

GNSS	Global Navigation Satellite System
TEC	Total Electron Content
PPEFs	Prompt Penetration Electric Fields
DDEFs	Disturbance Dynamo Electric Fields
MIT	Magnetosphere–Ionosphere–Thermosphere
TIDs	Traveling Ionospheric Disturbances

ESFs	Equatorial Spread-F
EIA	Equatorial Ionization Anomaly
HSS	High-Speed Solar Wind Streams
CMEs	Coronal Mass Ejections
GIMs	Global Ionosphere Maps

References

1. Gonzalez, W.D.; Tsurutani, B.T.; Clúa De Gonzalez, A.L. Interplanetary Origin of Geomagnetic Storms. *Space Sci. Rev.* **1999**, *88*, 529–562. [CrossRef]
2. Webb, D.F. Coronal Mass Ejections: The Key to Major Interplanetary and Geomagnetic Disturbances. *Rev. Geophys.* **1995**, *33*, 577–583. [CrossRef]
3. Zhang, J.; Richardson, I.G.; Webb, D.F.; Gopalswamy, N.; Hutrunen, E.; Kasper, J.C.; Nitta, N.V.; Poomvises, W.; Thompson, B.J.; Wu, C.C.; et al. Solar and Interplanetary Sources of Major Geomagnetic Storms (Dst ≤ -100 NT) during 1996–2005. *J. Geophys. Res. Space Phys.* **2007**, *112*, A10102. [CrossRef]
4. Burns, A.G.; Solomon, S.C.; Wang, W.; Killeen, T.L. The Ionospheric and Thermospheric Response to CMEs: Challenges and Successes. *J. Atmos. Sol. Terr. Phys.* **2007**, *69*, 77–85. [CrossRef]
5. Balan, N.; Liu, L.; Le, H. A Brief Review of Equatorial Ionization Anomaly and Ionospheric Irregularities. *Earth Planet. Phys.* **2018**, *2*, 257–275. [CrossRef]
6. Lu, G.; Goncharenko, L.P.; Richmond, A.D.; Roble, R.G.; Aponte, N. A Dayside Ionospheric Positive Storm Phase Driven by Neutral Winds. *J. Geophys. Res. Space Phys.* **2008**, *113*, A08304. [CrossRef]
7. Tsurutani, B.T.; Verkhoglyadova, O.P.; Mannucci, A.J.; Saito, A.; Araki, T.; Yumoto, K.; Tsuda, T.; Abdu, M.A.; Sobral, J.H.A.; Gonzalez, W.D.; et al. Prompt Penetration Electric Fields (PPEFs) and Their Ionospheric Effects during the Great Magnetic Storm of 30–31 October 2003. *J. Geophys. Res. Space Phys.* **2008**, *113*, A05311. [CrossRef]
8. Werner, S.; Bauske, R.; Prölss, G.W. On the Origin of Positive Ionospheric Storms. *Adv. Space Res.* **1999**, *24*, 1485–1489. [CrossRef]
9. Zhai, C.; Tang, S.; Peng, W.; Cheng, X.; Zheng, D. Driver of the Positive Ionospheric Storm over the South American Sector during 4 November 2021 Geomagnetic Storm. *Remote Sens.* **2023**, *15*, 111. [CrossRef]
10. Bojilova, R.; Mukhtarov, P.; Pancheva, D. Global Ionospheric Response During Extreme Geomagnetic Storm in May 2024. *Remote Sens.* **2024**, *16*, 4046. [CrossRef]
11. Balan, N.; Alleyne, H.; Otsuka, Y.; Lekshmi, D.V.; Fejer, B.G.; McCrea, I. Relative Effects of Electric Field and Neutral Wind on Positive Ionospheric Storms. *Earth Planets Space* **2009**, *61*, 439–445. [CrossRef]
12. Aa, E.; Chen, Y.; Luo, B. Dynamic Expansion and Merging of the Equatorial Ionization Anomaly During the 10–11 May 2024 Super Geomagnetic Storm. *Remote Sens.* **2024**, *16*, 4290. [CrossRef]
13. Blanc, M.; Richmond, A.D. The Ionospheric Disturbance Dynamo. *J. Geophys. Res. Space Phys.* **1980**, *85*, 1669–1686. [CrossRef]
14. Mansilla, G.A.; Zossi, M.M. Thermosphere–Ionosphere Response to a Severe Magnetic Storm: A Case Study. *Adv. Space Res.* **2012**, *49*, 1581–1586. [CrossRef]
15. Buonsanto, M.J. Ionospheric Storms—A Review. *Space Sci. Rev.* **1999**, *88*, 563–601. [CrossRef]
16. Gordiyenko, G.; Arikan, F.; Litvinov, Y.; Zhiganbaev, M. Ionospheric Response to the Extreme Geomagnetic Storm of 10–11 May 2024 Based on Total Electron Content Observations in the Central Asian and East Asian Regions. *Atmosphere* **2025**, *16*, 854. [CrossRef]
17. Lastovicka, J. Monitoring and Forecasting of Ionospheric Space Weather—Effects of Geomagnetic Storms. *J. Atmos. Sol. Terr. Phys.* **2002**, *64*, 697–705. [CrossRef]
18. Fuller-Rowell, T.J.; Millward, G.H.; Richmond, A.D.; Codrescu, M.V. Storm-Time Changes in the Upper Atmosphere at Low Latitudes. *J. Atmos. Sol. Terr. Phys.* **2002**, *64*, 1383–1391. [CrossRef]
19. Vijaya Lekshmi, D.; Balan, N.; Vaidyan, V.K.; Alleyne, H.; Bailey, G.J. Response of the Ionosphere to Super Geomagnetic Storms: Observations and Modeling. *Adv. Space Res.* **2008**, *41*, 548–555. [CrossRef]
20. Wang, W.; Lei, J.; Burns, A.G.; Solomon, S.C.; Wiltberger, M.; Xu, J.; Zhang, Y.; Paxton, L.; Coster, A. Ionospheric Response to the Initial Phase of Geomagnetic Storms: Common Features. *J. Geophys. Res. Space Phys.* **2010**, *115*, A07321. [CrossRef]
21. Nava, B.; Rodríguez-Zuluaga, J.; Alazo-Cuartas, K.; Kashcheyev, A.; Migoya-Orué, Y.; Radicella, S.M.; Amory-Mazaudier, C.; Fleury, R. Middle- and Low-Latitude Ionosphere Response to 2015 St. Patrick's Day Geomagnetic Storm. *J. Geophys. Res. Space Phys.* **2016**, *121*, 3421–3438. [CrossRef]
22. Bojilova, R.; Mukhtarov, P. Comparative Analysis of Global and Regional Ionospheric Responses during Two Geomagnetic Storms on 3 and 4 February 2022. *Remote Sens.* **2023**, *15*, 1739. [CrossRef]
23. Rukundo, W. The Ionospheric Dynamics of the African Sector Responding to a Severe Geomagnetic Storm; the Storm of 3–5 November 2021. *Space Weather* **2023**, *21*, e2022SW003219. [CrossRef]

24. Sreeja, V.; Devasia, C.V.; Ravindran, S.; Pant, T.K.; Sridharan, R. Response of the Equatorial and Low-Latitude Ionosphere in the Indian Sector to the Geomagnetic Storms of January 2005. *J. Geophys. Res. Space Phys.* **2009**, *114*, A06314. [CrossRef]
25. Simi, K.G.; Manju, G.; Haridas, M.K.M.; Nayar, S.R.P.; Pant, T.K.; Alex, S. Ionospheric Response to a Geomagnetic Storm during November 8–10, 2004. *Earth Planets Space* **2012**, *65*, 343–350. [CrossRef]
26. Chakraborty, M.; Kumar, S.; Kumar De, B.; Guha, A. Effects of Geomagnetic Storm on Low Latitude Ionospheric Total Electron Content: A Case Study from Indian Sector. *J. Earth Syst. Sci.* **2015**, *124*, 1115–1126. [CrossRef]
27. Paul, B.; Gordiyenko, G.; Galav, P. Study of the Low and Mid-Latitude Ionospheric Response to the Geomagnetic Storm of 20th December 2015. *Astrophys. Space Sci.* **2020**, *365*, 174. [CrossRef]
28. Vankadara, R.K.; Panda, S.K.; Amory-Mazaudier, C.; Fleury, R.; Devananboyina, V.R.; Pant, T.K.; Jamjareegulgarn, P.; Haq, M.A.; Okoh, D.; Seemala, G.K. Signatures of Equatorial Plasma Bubbles and Ionospheric Scintillations from Magnetometer and GNSS Observations in the Indian Longitudes during the Space Weather Events of Early September 2017. *Remote Sens.* **2022**, *14*, 652. [CrossRef]
29. Rajana, S.S.K.; Panda, S.K.; Jade, S.; Vivek, C.G.; Upadhayaya, A.K.; Bhardwaj, A.; Jorphail, S.; Seemala, G.K. Impact of Two Severe Geomagnetic Storms on the Ionosphere over Indian Longitude Sector during March–April 2023. *Astrophys. Space Sci.* **2024**, *369*, 3. [CrossRef]
30. Chougule, P.; Iswariya, S.; Rajana, S.S.K.; Shetti, D.; Chougule, S.; Vivek, C.G.; Dabbakuti, J.R.K.K.; Maurya, A.K.; Sasmal, S.; Panda, S.K. Peculiar Storm-Time Dynamics of the Summer Solstice Ionosphere over the Indian Region During the June 2025 Geomagnetic Storm. *Atmosphere* **2026**, *17*, 189. [CrossRef]
31. Seemala, G.K. Estimation of Ionospheric Total Electron Content (TEC) from GNSS Observations. In *Atmospheric Remote Sensing: Principles and Applications*; Elsevier: Amsterdam, The Netherlands, 2022; pp. 63–84. [CrossRef]
32. Wood, A.G.; Alfonsi, L.; Clausen, L.B.N.; Jin, Y.; Spogli, L.; Urbář, J.; Rawlings, J.T.; Whittaker, I.C.; Dorrian, G.D.; Høeg, P.; et al. Variability of Ionospheric Plasma: Results from the ESA Swarm Mission. *Space Sci. Rev.* **2022**, *218*, 52. [CrossRef]
33. Manoj, C.; Maus, S.; Lühr, H.; Alken, P. Penetration Characteristics of the Interplanetary Electric Field to the Daytime Equatorial Ionosphere. *J. Geophys. Res. Space Phys.* **2008**, *113*, A12310. [CrossRef]
34. Kelley, M.C.; Vlasov, M.N.; Foster, J.C.; Coster, A.J. A Quantitative Explanation for the Phenomenon Known as Storm-Enhanced Density. *Geophys. Res. Lett.* **2004**, *31*, L19809. [CrossRef]
35. de Abreu, A.J.; Correia, E.; Macho, E.P.; Venkatesh, K.; de Jesus, R.; Pignalberi, A.; Pezzopane, M.; Pillat, V.G.; Fagundes, P.R.; Gende, M. Electrodynamics and Ionospheric Irregularities during Intense Geomagnetic Storm That Occurred in March 2024 over American and Antarctic Sectors. *Adv. Space Res.* **2026**, *78*, 1427–1451. [CrossRef]
36. Balan, N.; Otsuka, Y.; Nishioka, M.; Liu, J.Y.; Bailey, G.J. Physical Mechanisms of the Ionospheric Storms at Equatorial and Higher Latitudes during the Recovery Phase of Geomagnetic Storms. *J. Geophys. Res. Space Phys.* **2013**, *118*, 2660–2669. [CrossRef]
37. Lei, J.; Wang, W.; Burns, A.G.; Solomon, S.C.; Richmond, A.D.; Wiltberger, M.; Goncharenko, L.P.; Coster, A.; Reinisch, B.W. Observations and Simulations of the Ionospheric and Thermospheric Response to the December 2006 Geomagnetic Storm: Initial Phase. *J. Geophys. Res. Space Phys.* **2008**, *113*, A01314. [CrossRef]
38. Cai, X.; Burns, A.G.; Wang, W.; Qian, L.; Solomon, S.C.; Eastes, R.W.; Pedatella, N.; Daniell, R.E.; McClintock, W.E. The Two-Dimensional Evolution of Thermospheric $\sum O/N_2$ Response to Weak Geomagnetic Activity During Solar-Minimum Observed by GOLD. *Geophys. Res. Lett.* **2020**, *47*, e2020GL088838. [CrossRef]
39. Yu, T.; Wang, W.; Ren, Z.; Cai, X.; He, M. Vertical Variations in Thermospheric O/N_2 and the Relationship Between O and N_2 Perturbations During a Geomagnetic Storm. *Earth Space Sci.* **2023**, *10*, e2023EA002988. [CrossRef]
40. Zhang, Y.; Paxton, L.J.; Morrison, D.; Marsh, D.; Kil, H. Storm-Time Behaviors of O/N_2 and NO Variations. *J. Atmos. Sol. Terr. Phys.* **2014**, *114*, 42–49. [CrossRef]
41. Chakraborty, S.; Ray, S.; Sur, D.; Datta, A.; Paul, A. Effects of CME and CIR induced geomagnetic storms on low-latitude ionization over Indian longitudes in terms of neutral dynamics. *Adv. Space Res.* **2020**, *65*, 198–213. [CrossRef]
42. Sur, D.; Ray, S.; Paul, A. High and Mid Latitude and near Subsolar Point Ionospheric and Thermospheric Responses to the Solar Flares and Geomagnetic Storms during Low Solar Activity Periods of 2017 and 2020. *Adv. Space Res.* **2022**, *70*, 157–178. [CrossRef]

Disclaimer/Publisher's Note: The statements, opinions and data contained in all publications are solely those of the individual author(s) and contributor(s) and not of MDPI and/or the editor(s). MDPI and/or the editor(s) disclaim responsibility for any injury to people or property resulting from any ideas, methods, instructions or products referred to in the content.